

Retrieval of vertical concentration profiles from OSIRIS UV-visible limb spectra

K. Strong, B.M. Joseph, R. Dosanjh, I.C. McDade, C.A. McLinden, J.C. McConnell, J. Stegman, D.P. Murtagh, and E.J. Llewellyn

Abstract: The OSIRIS instrument, launched on the Odin satellite in February 2001, includes an optical spectrograph that will record UV-visible spectra of sunlight scattered from the limb over a range of tangent heights. These spectra will be used to retrieve vertical profiles of ozone, NO₂, OClO, BrO, NO₃, O₂, and aerosols, for the investigation of both stratospheric and mesospheric processes, particularly those related to ozone chemistry. In this work, the retrieval of vertical profiles of trace-gas concentrations from OSIRIS limb-radiance spectra is described. A forward model has been developed to simulate these spectra, and it consists of a single-scattering radiative-transfer model with partial spherical geometry, trace-gas absorption, Mie scattering by stratospheric aerosols, a Lambertian surface contribution, and OSIRIS instrument response and noise. Number-density profiles have been retrieved by using optimal estimation (OE) to combine an a priori profile with the information from sets of synthetic "measurements". For ozone, OE has been applied both to limb radiances at one or more discrete wavelengths and to effective-column abundances retrieved over a broad spectral range using differential optical absorption spectroscopy (DOAS). The results suggest that, between 15 and 35 km, ozone number densities can be retrieved to 10% accuracy or better on 1 and 2 km grids and to 5% on a 5 km grid. The combined DOAS-OE approach has also been used to retrieve NO₂ number densities, yielding 13% accuracy or better for altitudes from 18 to 36 km on a 2 km grid. Differential optical absorption spectroscopy – optimal estimation retrievals of BrO and OClO reproduce the true profiles above 15 km in the noise-free case, but the quality of the retrievals is highly sensitive to noise on the simulated OSIRIS spectra because of the weak absorption of these two gases. The development of inversion methods for the retrieval of trace-gas concentrations from OSIRIS spectra is

Received 25 January 2000. Accepted 25 December 2000. Published on the NRC Research Press Web site at <http://cjp.nrc.ca/> on 18 April 2002.

K. Strong,¹ B.M. Joseph, and R. Dosanjh. Department of Physics, University of Toronto, 60 St. George Street, Toronto, ON M5S 1A7, Canada.

I.C. McDade and J.C. McConnell. Department of Earth and Atmospheric Science, York University, 4700 Keele Street, Toronto, ON M3J 1P3, Canada.

C.A. McLinden.² Department of Earth System Science, University of California at Irvine, Irvine, CA 92697-3100, U.S.A.

J. Stegman and D.P. Murtagh. Department of Meteorology, Stockholm University, Stockholm, S-106 91, Sweden.

E.J. Llewellyn. Department of Physics and Engineering Physics, University of Saskatchewan, 116 Science Place, Saskatoon, SK S7N 5E2, Canada.

¹Corresponding author (email: strong@atmosph.physics.utoronto.ca).

²Present Address: Department of Physics and Astronomy, York University, 4700 Keele Street, Toronto, ON M3J 1P3, Canada.

continuing, and a number of future improvements to the forward model and refinements of the retrieval algorithms are identified.

PACS Nos.: 42.68Mj, 94.10Dy

Résumé : L'instrument OSIRIS a été lancé en février 2001 à bord du satellite Odin comprend un spectrographe optique pour enregistrer le spectre UV-visible de la lumière solaire diffusée par le limbe terrestre et ce, le long de tangentes à plusieurs altitudes. Les spectres obtenus servent à recouvrer les profils verticaux de O₃, NO₂, OCIO, BrO, NO₃ et O₂ ainsi que d'aérosols, afin d'étudier les processus stratosphériques et mésosphériques, surtout ceux reliés à la chimie de l'ozone. Nous décrivons ici comment recouvrer les profils verticaux de concentration des gaz mineurs à partir des mesures de radiance du limbe par OSIRIS. Nous avons développé un modèle pour simuler ces spectres. C'est un modèle de transfert radiatif à diffusion simple dans une géométrie sphérique partielle et qui tient compte de l'absorption par les gaz apparaissant sous forme de trace, de la diffusion de Mie par les aérosols stratosphériques, d'une contribution de surface de Lambert et de la réponse et du bruit inhérents à l'appareil OSIRIS. Nous avons recouvré des profils de densité par estimation optimale (OE) afin de combiner des profils a priori avec les résultats de mesures sur un modèle (précurseur). Pour l'ozone, nous avons appliqué l'OE à la fois au rayonnement du limbe à une ou plusieurs longueurs d'onde et aux profils verticaux d'abondance obtenus sur une large bande spectrale en utilisant la spectroscopie par absorption optique différentielle (DOAS). Les résultats suggèrent qu'entre 15 et 35 km d'altitude, on peut déterminer la densité de l'ozone avec une précision de 10% ou mieux sur une grille de pas de 1–2 km et de 5% sur une grille de 5 km. Nous avons utilisé l'approche combinée DOAS-OE pour recouvrer les valeurs de densité du NO₂ aussi, avec une précision de 13% ou mieux, entre 18 et 36 km d'altitude sur une grille de 2 km. La méthode DOAS-OE recouvre les vrais profils pour les composés BrO et OCIO au dessus de 15 km dans le cas où il n'y a pas de bruit, mais la qualité des résultats est très sensible au bruit sur les spectres OSIRIS simulés à cause de la faible absorption des deux gaz. Nous continuons à développer les méthodes d'inversion pour recouvrer les concentrations des gaz présents sous forme de trace à partir des spectres d'OSIRIS et nous avons déjà identifié les futures améliorations à apporter au modèle précurseur.

[Traduit par la Rédaction]

1. Introduction

Odin is a joint astronomy/aeronomy satellite that was launched on 20 February 2001 carrying two instruments, a sub-millimetre radiometer (SMR) and a combined optical spectrograph and infrared imager (OSIRIS) [1]. Odin was launched into a Sun-synchronous polar orbit at 97.8° inclination and 600 km altitude, with the ascending node crossing the equator at 18:00 LT. The satellite has two viewing modes, a space-staring mode for astronomy and a limb-scanning mode for aeronomy. The OSIRIS instrument is being used only for atmospheric observations, viewing the limb of the atmosphere in the orbital plane, and up to 32° away from this plane. The spacecraft can be scanned through a range of tangent altitudes, from 10 km to as high as 120 km, at up to 40 scans per orbit. The OSIRIS optical spectrograph records spectra of sunlight scattered from the limb, covering the UV-visible spectral range from 280 to 800 nm. These spectra will be used to retrieve stratospheric vertical profiles of ozone, NO₂, OCIO, BrO, NO₃, O₂, and aerosols, for the investigation of both stratospheric and mesospheric processes, particularly those related to ozone chemistry [2]. In contrast, the infrared imager simultaneously images emission features at 1.27 μm from a range of tangent heights for the retrieval of vertical profiles of atomic oxygen and ozone in both the stratosphere and the mesosphere [3].

Limb sounding is a well-established technique for measuring atmospheric composition. Limb-viewing geometry provides good vertical resolution and significant enhancement of the atmospheric path, thereby increasing the sensitivity to weakly absorbing trace gases. It also has the advantage of a background that is either a direct source (e.g., Sun, stars) or space (cold and uniform) rather than the surface of the Earth (hot and variable). However, limb-sounding observations have lower horizontal

resolution and are generally limited to the upper troposphere and above. In addition, they require precise information about the field-of-view and spacecraft attitude so that the pointing can be accurately determined.

Most previous limb-sounding satellite instruments have made occultation or emission measurements at infrared or microwave wavelengths to measure atmospheric composition (e.g., LIMS [4], ISAMS [5], MLS [6]). In the UV-visible spectral region, space-based instruments have relied on nadir observations of back-scattered solar radiation at a number of specific wavelengths (e.g., TOMS [7], BUV and SBUV [8]) or have made solar occultation measurements in the limb, again at several discrete wavelengths (e.g., SAGE I and II [9]). The SPEAM instrument, flown on the Space Shuttle in 1984 and 1992, made visible and near-infrared measurements of ozone and nitrogen compounds using limb-scanning solar occultation [10]. More recently, the nadir-viewing GOME instrument, launched on ERS-2 in April 1995, has been used to retrieve ozone, NO₂, SO₂, BrO, and OClO from UV-visible spectra recorded between 237 and 794 nm [11,12].

Space-based observations of radiation scattered from the limb (rather than limb emission, limb occultation, or nadir back-scatter measurements) are fewer because of the complexity of the viewing geometry, particularly if multiple scattering is taken into account. The solar mesosphere explorer (SME), launched in 1981, carried the first satellite instruments to make such measurements: mesospheric ozone profiles were retrieved using the ultraviolet spectrometer [13], while stratospheric NO₂ profiles were retrieved using the visible spectrometer [14]. Both instruments recorded altitude profiles of scattered sunlight in two spectral channels (265/296.4 nm and 439/442 nm), and a single-scattering radiative-transfer model was used for the inversion of the data. The impact of multiple scattering on limb observations in the UV was examined by Aruga and Heath [15], who used a Monte Carlo model to simulate the limb radiances. Two recently launched instruments are being used to further investigate the potential for retrieving stratospheric ozone profiles from UV-visible limb spectra of scattered sunlight. The MSX satellite, launched in April 1996 with a 5 year lifetime, carries a suite of UV-visible sensors (UVISI) that will observe the limb from 110 to 900 nm [16]. This was followed by a Space Shuttle flight of the SOLSE instrument in November/December 1997. SOLSE imaged the limb onto a charge-coupled-device detector array through a spectrometer to simultaneously obtain spectra from 260 to 350 nm at a range of tangent heights; analysis of these spectra is currently underway [17,18].

OSIRIS will thus be one of the first instruments to measure broadband UV-visible spectra of scattered sunlight in the limb for the retrieval. This technique is currently of considerable interest [19], with similar UV-visible limb measurements planned for SAGE III [20] and SCIAMACHY [21]. In this paper, we discuss one approach to the retrieval of vertical profiles of concentration from these spectra, focusing on ozone in the stratosphere. We apply the optimal estimation method both to the limb radiances and to the effective slant columns that will be obtained by the optical spectrograph as a function of tangent height.

2. The OSIRIS forward model

2.1. Limb-radiance calculation

Development of retrieval algorithms for the OSIRIS optical spectrograph first requires a radiative-transfer model to simulate the anticipated OSIRIS UV-visible limb-radiance spectra. An ideal forward model should meet the following criteria:

- (i) cover the relevant spectral range with sufficient spectral resolution;
- (ii) include absorption features of all relevant trace gases;
- (iii) use spherical geometry;
- (iv) have reliable input parameters, including the neutral atmosphere, the solar spectrum, absorption cross sections, and vertical profiles of the minor species;

- (v) give an accurate description of multiple-scattering processes;
- (vi) where important, include polarization, the Ring effect, refraction, aerosols, airglow, and surface albedo effects;
- (vii) include an appropriate instrument response function; and
- (viii) be fast for use in retrieval calculations.

The forward model used in this study was developed specifically for OSIRIS and is a relatively simple single-scattering model. This gives it the advantage of computational speed and, therefore, makes it particularly useful, for example, in optimal estimation calculations, where a forward model is currently run repeatedly to generate a weighting-function matrix. While a full radiative-transfer model would include multiple scattering, calculations performed with the MODTRAN 3.5 model [22] for 90° scattering angle (OSIRIS viewing geometry) by Lehtinen [23] indicate that multiple scattering contributes less than 6% to the total radiance above a tangent height of 20 km. This increases to 25% of the total if the scattering angle is decreased to about 60° and the tangent point is in bright sunlight.

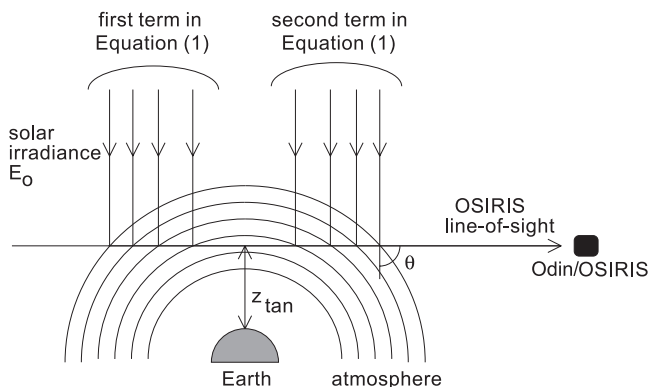
The single-scattering model used in this study employs partial spherical geometry, including the curvature of the Earth for both incoming and outgoing radiation. It is used to calculate the extinction of the incoming solar radiation from the top of the atmosphere (120 km) down to a scattering layer using a 0.5 km altitude grid. This vertical grid provides an accurate calculation of the radiance near the tangent point. The model includes extinction of the incoming solar radiation and the outgoing scattered radiation by ozone, NO₂, OClO, and BrO absorption, and by Rayleigh and Mie scattering. Limb radiances in the OSIRIS viewing direction are generated for radiation that travels from the top of the atmosphere down to a given tangent height (between 10 and 120 km) and is then scattered out towards OSIRIS.

The general equation for the singly scattered limb-radiance I , at some wavelength λ and tangent height z_{tan} , is thus

$$\begin{aligned}
 I(\lambda, z_{\text{tan}}) &= E_0(\lambda) \int_{\text{line of sight}} \tau_{\text{in}}(\lambda, \infty : z) S(\lambda, z, \theta) \tau_{\text{out}}(\lambda, z : \infty) dz \\
 &= E_0(\lambda) \int_{\infty}^{z_{\text{tan}}} \tau_{\text{in}}(\lambda, \infty : s(z)) S(\lambda, z, \theta) \tau_{\text{out}}(\lambda, s(z) : \infty) ds(z) \\
 &\quad + E_0(\lambda) \int_{z_{\text{tan}}}^{\infty} \tau_{\text{in}}(\lambda, \infty : s(z)) S(\lambda, z, \theta) \tau_{\text{out}}(\lambda, s(z) : \infty) ds(z) \quad (1)
 \end{aligned}$$

where $E_0(\lambda)$ is the solar irradiance incident on the top of the atmosphere (photons cm⁻² s⁻¹ Å⁻¹), $\tau_{\text{in}}(\lambda, \infty : z)$ is the atmospheric transmission in from the top of the atmosphere to the scattering point at altitude z along the OSIRIS line of sight, $S(\lambda, z, \theta)$ is a scattering term describing the proportion of solar irradiance singly scattered into the instrument line of sight, θ is the forward scattering angle, $\tau_{\text{out}}(\lambda, z : \infty)$ is the atmospheric transmission back out from the scattering point at altitude z along the OSIRIS line of sight to the top of the atmosphere, and $s(z)$ denotes the altitude-dependent slant path along the line of sight. The integral along the line of sight is broken down into two terms, corresponding to solar irradiance incident on the atmosphere (*i*) beyond the tangent point and (*ii*) between the tangent point and the satellite, as illustrated in Fig. 1 for a scattering angle of 90°.

Fig. 1. Schematic view of OSIRIS limb-viewing geometry for a scattering angle of 90°.



Substituting in the appropriate expressions, this equation becomes

$$\begin{aligned}
 I(\lambda, z_{\text{tan}}) = & E_0(\lambda) \int_{\infty}^{z_{\text{tan}}} \exp \left\{ - \int_{\infty}^z k(\lambda, z') ds(z') \right\} \\
 & \times \left\{ \frac{1}{4\pi} \right\} \left\{ P(D, \theta) k^{\text{scat}}(\lambda, z) \right\} \exp \left\{ - \int_z^{\infty} k(\lambda, z'') ds(z'') \right\} ds(z) \\
 & + E_0(\lambda) \int_{z_{\text{tan}}}^{\infty} \exp \left\{ - \int_{\infty}^z k(\lambda, z') ds(z') \right\} \\
 & \times \left\{ \frac{1}{4\pi} \right\} \left\{ P(D, \theta) k^{\text{scat}}(\lambda, z) \right\} \exp \left\{ - \int_z^{\infty} k(\lambda, z'') ds(z'') \right\} ds(z) \quad (2)
 \end{aligned}$$

In this equation,

$$k(\lambda, z) = k^{\text{scat}}(\lambda, z) + k^{\text{abs}}(\lambda, z) = [\sigma_{\text{Ray}}(\lambda)N(z) + k_{\text{Mie}}(\lambda, z)] + \sum_i \sigma_i(\lambda)N_i(z) \quad (3)$$

is the total volume extinction coefficient (cm⁻¹) due to the combination of Rayleigh and Mie scattering and absorption by trace gases, where $\sigma_{\text{Ray}}(\lambda)$ is the Rayleigh-scattering cross section (cm²/molecule), $N(z)$ is atmospheric number density (molecules/cm³), $k_{\text{Mie}}(\lambda, z)$ is the volume extinction coefficient due to Mie scattering (cm⁻¹), $\sigma_i(\lambda)$ is the absorption cross section of trace-gas i (cm²/molecule), and $N_i(z)$ is the number density of trace-gas i (molecules/cm³). Also,

$$P(D, \theta) = \frac{k_{\text{Ray}}^{\text{scat}}(D)}{k_{\text{Ray}}^{\text{scat}}(D) + k_{\text{Mie}}^{\text{scat}}(D)} P_{\text{Ray}}(\theta) + \frac{k_{\text{Mie}}^{\text{scat}}(D)}{k_{\text{Mie}}^{\text{scat}}(D) + k_{\text{Ray}}^{\text{scat}}(D)} P_{\text{Mie}}(\theta) \quad (4)$$

is the effective phase function, which is an altitude-dependent Rayleigh–Mie weighted average, where $k_{\text{Ray}}^{\text{scat}}(D)$ and $k_{\text{Mie}}^{\text{scat}}(D)$ are the Rayleigh and Mie volume-scattering coefficients at vertical optical depth D , and $P_{\text{Ray}}(\theta)$ and $P_{\text{Mie}}(\theta)$ are the Rayleigh and Mie single-scattering phase functions, respectively.

The calculation of the Rayleigh molecular-scattering terms follows the approach of Witt et al. [24]. The scattering cross section in cm²/molecule is given by Penndorf [25] as

$$\sigma_{\text{Ray}}(\lambda) = \frac{32\pi^3}{3\lambda^4} \frac{[n_0(\lambda) - 1]^2}{N_0^2} \frac{6 + 3\rho_n(\lambda)}{6 - 7\rho_n(\lambda)} \quad (5)$$

where $n_0(\lambda)$ is the refractive index of standard air, based on eq. (2) of Edlen [26], and N_0 is the number density of air, taken to be $2.54743 \times 10^{19} \text{ cm}^{-3}$ for 15°C and $\rho_n = 0.035$ [25]. The depolarization factor is

$$\rho_n(\lambda) = 6 \times \frac{F_K(\lambda) - 1}{3 + 7F_K(\lambda)} \quad (6)$$

The King correction factor for air is given by (see, for example, Bates [27])

$$F_K(\lambda) = 1.0367 + (5.381 \times 10^{-12})\bar{\nu}_{\text{vac}}^2 + (0.304 \times 10^{-20})\bar{\nu}_{\text{vac}}^4 \quad (7)$$

where $\bar{\nu}_{\text{vac}}$ is the wave number in a vacuum (cm^{-1}). The Rayleigh-scattering phase function is calculated using (Goody and Yung, p. 298 of ref. 28)

$$P_{\text{Ray}}(\theta) = 2 \frac{0.75}{2 + \rho_n} \left[1 + \rho_n + (1 - \rho_n) \cos^2 \theta \right] \quad (8)$$

Mie scattering by stratospheric aerosols is also included in the radiative-transfer model. Three aerosol profiles (from 10 to 120 km) have been implemented, using data from MODTRAN [22]: background stratospheric, fresh volcanic, and aged volcanic. A single extinction profile is given for each scenario at 500 nm, and scaling factors are supplied at 337 and 694 nm. Scaling factors at any other wavelength are determined through parabolic interpolation (or extrapolation). Similarly, the Mie phase function for 90° scattering is given at 337, 550, and 694 nm, and parabolic wavelength interpolation/extrapolation is again used. The altitude-dependent effective phase function, $P(D, \theta)$, is used as defined in (4).

2.2. Addition of a Lambertian surface

A Lambertian surface is included in the forward model in such a way that it can reasonably represent the physics of the situation without requiring a large amount of additional calculation. The situation is shown in Fig. 2. The “direct” solar radiance, attenuated through the atmosphere and scattered into the OSIRIS line-of-sight, is calculated as above. The analogous surface component is then determined as follows. First, the surface albedo, Λ , is defined as

$$\Lambda = \frac{E^\uparrow(D_1)}{E^\downarrow(D_1)} \quad (9)$$

where $E^\uparrow(D_1)$ and $E^\downarrow(D_1)$ are the upward and downward irradiances at the surface, respectively, and D_1 is the total vertical optical depth of the atmosphere. If the surface is Lambertian, then the up-welling surface radiance, I_s , is a constant given by

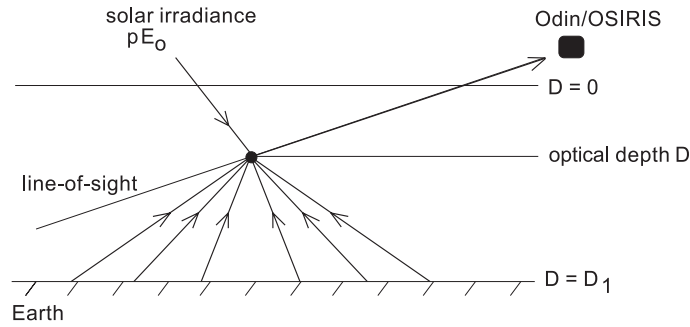
$$I_s = \frac{E^\uparrow(D_1)}{\pi} = \frac{\Lambda E^\downarrow(D_1)}{\pi} \quad (10)$$

From Fig. 2, the surface component of the radiance in a plane-parallel atmosphere, singly scattered into the satellite line of sight (LOS) at optical depth D is given by

$$I_{\text{LOS}}(D) = I_s \int_0^{2\pi} \int_0^1 P(\theta) \exp \left[- \left(\frac{D_1 - D}{\mu} \right) \right] d\mu d\phi \quad (11)$$

where μ is the cosine of the zenith angle. If $P(\theta)$ is slowly varying, then it can be replaced with the constant phase function, \bar{P} , and the expression becomes

$$I_{\text{LOS}}(D) = 2\pi I_s \bar{P} E_2(D_1 - D) \quad (12)$$

Fig. 2. Schematic view of the geometry used to calculate the surface component included in the forward model.

At present, \bar{P} is taken as the effective phase function at 90° , although improvements to this are being investigated. There is no azimuthal dependence, and the remaining integral is recognized as an exponential integral of order two, denoted as $E_2(D_1 - D)$. Polynomial approximations for exponential integrals exist that have an accuracy of 0.01% or better [29],

$$E_2(x) = \begin{cases} e^{-x} - x(0.577\,216 + 0.999\,992x - 0.249\,911x^2 + 0.055\,1997x^3 \\ \quad - 0.009\,76004x^4 + 0.001\,07857x^5 - \ln\{x\}) & \text{for } 0 < x \leq 1 \\ e^{-x} \frac{1.430\,913 + 0.995\,924x}{1.681\,534 + 3.330\,657x + x^2} & \text{for } x > 1 \end{cases} \quad (13)$$

In terms of the down-welling irradiance,

$$I_{\text{LOS}}(D) = 2\Lambda E^\downarrow(D_1) \bar{P} E_2(D_1 - D) \quad (14)$$

The accuracy of the two approximations made, namely the use of \bar{P} and a plane-parallel atmosphere, increases with altitude as the integral becomes dominated by the near-nadir radiances due to the increasing slant optical depths experienced by radiances in other directions. For similar reasons, these approximations are better at shorter wavelengths. Finally, the down-welling irradiance is the sum of the direct and the diffuse. The direct is already calculated but the diffuse is not. Instead, the following parameterization is used as a proxy for the diffuse (adapted from Sturm [30])

$$E_{\text{diffuse}}^\downarrow(D_1) = \mu_0 \pi F_0 \exp\left(\frac{D_1}{\mu_0}\right) \left[\frac{\mu_0 \exp(D^s/\mu_0)}{\mu_0 + (1 - \eta)D^s} - 1 \right] \quad (15)$$

where πF_0 is the direct solar flux, D^s refers to the total vertical scattering optical depth, and η is the fraction of light scattered into the forward hemisphere.

As with the single-scattered radiance, given in (2), the surface-reflected radiance must be attenuated from the point at which it scatters into the line-of-sight to the top of the atmosphere. It is incorporated into the solution through two additional terms in (2), one for each side of the tangent point.

To obtain some idea of how the surface contribution affects the total radiance, consider the case of a conservative and (near) nonscattering atmosphere. The fractional increase due to the surface contribution can be shown to be $2\Lambda\mu_0$. For a near-overhead Sun and a highly reflecting surface, the surface contribution can be as large as (or larger than) the atmospheric component. For typical Odin geometry, $\mu_0 = \cos^{-1}(80^\circ) = 0.17$ and $\Lambda = 0.3$, there would be a modest 10% increase. Note, however, that the absorption signature in the surface-reflected radiance may be larger than the atmospheric component as it passes completely through the atmosphere at least once.

2.3. Forward-model input parameters

The radiative-transfer model requires a number of input parameters. The SMR reference atmosphere [31] has been adopted for vertical profiles of air density, ozone, the NO₂-mixing ratio, pressure, temperature, and density from 0 to 120 km. Profiles of the BrO- and OCIO-mixing ratio have been constructed from 0 to 100 km. MODTRAN3 stratospheric aerosol profiles are used from 10 to 120 km as described above. All input profiles have been converted onto a 0.5 km altitude grid.

The solar irradiance spectrum is taken from MODTRAN3 [22]. It is based on the *Solar flux atlas* of Kurucz et al. [32] and covers the full OSIRIS spectral range of 280 to 800 nm at a spectral resolution of 5 cm⁻¹. UV-visible absorption cross sections for ozone at 221 K [33], NO₂ at 221 K [34], BrO at 223 K [35], and OCIO at 204 K [36] are used, and all four are initially binned onto a 0.1 nm wavelength grid. The absolute experimental uncertainties in these cross sections are 2.6% for ozone, 2.3% for NO₂, 7–8% for BrO, and 4 × 10⁻¹⁹ cm² for OCIO [33–36].

The scattering angle, solar zenith angle, and surface albedo are variable parameters; however, for this work these were generally fixed. A scattering angle of 90° was used, as this is appropriate for the Odin/OSIRIS orbital geometry. Typical values of 80° for the solar zenith angle and 0.3 for the surface albedo were adopted.

2.4. The OSIRIS instrument function

To simulate fully the anticipated OSIRIS limb-radiance spectra, a model of the instrument function is applied to the output of the single-scattering radiative-transfer model. As described in ref. 3, the OSIRIS optical spectrograph design uses offset parabolic reflectors with an aspherical-ruled reflection grating. It has a single input slit, oriented horizontally; this provides a field-of-view that is 1 km (vertical) × 18 km (horizontal), with a spatial resolution of 1 km at the limb. The reflection grating (Jobin–Yvon) is ruled at 600 grooves/mm, blazed at 400 nm, and used in first order. The detector is a charge-coupled device (EEV CCD26), back-thinned for higher quantum efficiency, and multipinned phase for low dark current. It consists of 1353 pixels × 143 pixels, each pixel being 20 μm × 27 μm in size; of this, a region 1353 pixels across by 32 pixels high will be used for OSIRIS measurements. This combination of grating and detector provides spectral coverage of 280–800 nm, at a spectral resolution of 1 nm for 280–450 nm and 2 nm for 450–800 nm, with a sampling of 2.4 pixels/nm. The anticipated minimum sensitivity is 12 000 Rayleigh Å⁻¹ pixel⁻¹ (where 1 Rayleigh = 10⁶/4π photons s⁻¹ cm⁻² sr⁻¹).

The model of the OSIRIS instrument-response function includes the wavelength-dependent grating efficiency, the wavelength-dependent CCD quantum efficiency, the reflectances of the four mirrors, the order sorter, and the antireflection coatings, the input solid angle and field-of-view, the pixel bandwidth, the spectral resolution, and the spectral sampling. The signal, $S(\lambda)$ in counts s⁻¹ pixel⁻¹, output by OSIRIS is determined as follows:

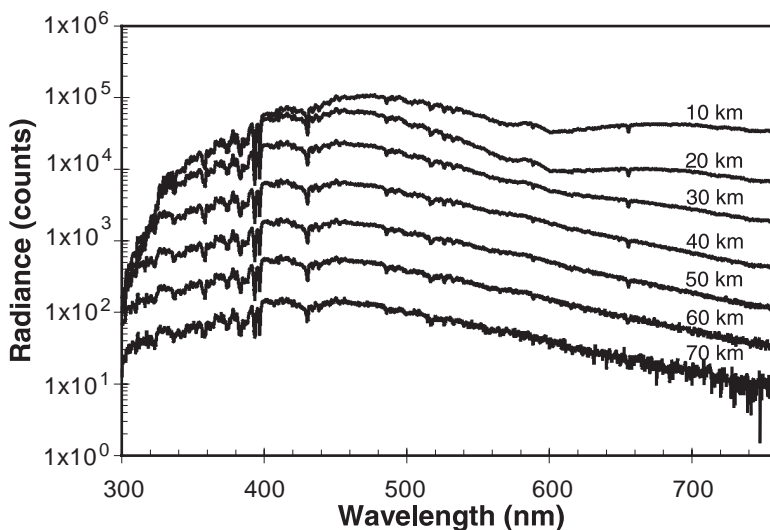
$$S(\lambda) = \frac{10^7}{4\pi} I(\lambda) \frac{A\Omega}{G} Q_{\text{CCD}}(\lambda) \frac{d\lambda}{dp} \frac{1}{N_{\text{col}}} \tau(\lambda) \quad (16)$$

where 10⁷/4π is a conversion from Rayleigh/Å to photons s⁻¹ cm⁻² sr⁻¹ nm⁻¹, A is the area of the OSIRIS objective telescope (11.88 cm²), Ω is the solid angle subtended by the OSIRIS field-of-view (sr), G is the CCD gain (14 electrons/count), $Q_{\text{CCD}}(\lambda)$ is the CCD quantum efficiency (electrons/photon), $d\lambda/dp$ is the instrument dispersion (0.384 nm/pixel), and N_{col} is the number of pixels in a column of the CCD (32 pixels). The instrument transmission or throughput is

$$\tau(\lambda) = E_{\text{grating}}(\lambda) R_{\text{mirror}}^4 R_{\text{coating}}^2 E_{\text{sorter}} \quad (17)$$

with $E_{\text{grating}}(\lambda)$ as the grating efficiency, R_{mirror} as the mirror reflectance (0.95 for each of four surfaces), R_{coating} as the coating reflectance (0.985 for each of two surfaces), and E_{sorter} as the order-sorter efficiency (0.80). Values obtained during calibration testing of the optical spectrograph development

Fig. 3. Limb-radiance spectra generated as a function of tangent height with the forward model using background aerosol, albedo = 0.3, SZA = 80°, scattering angle = 90°, and the OSIRIS Development Model instrument response and noise.



model (DM) have been used for the modelling in this work. A Gaussian instrument line shape with a full-width half-maximum of 1.0 nm was applied to smooth the simulated radiances to OSIRIS spectral resolution.

In addition, realistic noise from the OSIRIS DM calibration measurements has been incorporated into the forward model, using

$$N = \sqrt{N_{\text{shot}}^2 + N_{\text{dark current}}^2 + N_{\text{readout}}^2 + N_{\text{output gate}}^2} \quad (18)$$

which combines noise terms due to shot noise, dark current, CCD readout, and output gate. Values of 25 and 10 electrons were used for the readout noise and the output gate, respectively. The CCD dark current was set at 17 electrons pixel⁻¹ s⁻¹. Figure 3 shows some typical limb-radiance spectra generated as a function of tangent height with the DM instrument response and noise applied, assuming a single pixel for each wavelength bin and an integration time of 1 s.

3. OSIRIS retrieval algorithms

3.1. Optimal estimation

The goal of the retrieval process is to use the OSIRIS limb radiances to obtain the local vertical concentration profiles of ozone, NO₂, BrO, and OClO (in molecules/cm³) as a function of altitude. This involves the use of a discrete set of measurements with some error covariance to determine a trace-gas profile, which is a continuous variable. In this study, the technique of optimal estimation (OE) has been adopted. Optimal estimation provides an elegant method of combining a priori information about a constituent profile with measurements to retrieve the best estimate of the true profile and its error covariance. The details of the OE method have been described by Rodgers [37,38] and are briefly reviewed here. This approach has general applicability and has been used, for example, in the retrieval of vertical profiles from the GOME and SOLSE/LORE instruments [18,39].

The retrieval and characterization of the system starts with the definition of a forward model F that relates a vector of m measurements, y , to an atmospheric state vector x defined at n levels

$$y = F(x, b) + \varepsilon \quad (19)$$

where \mathbf{b} is a vector of model parameters, and ε is the measurement error, assumed to be normally distributed about zero with error covariance S_y . In the case of OSIRIS, \mathbf{x} is the vertical concentration profile of the atmospheric species of interest, and measurements \mathbf{y} (obtained at m tangent heights) are either limb radiances or effective-column abundances obtained using differential optical absorption spectroscopy (DOAS) (discussed below). For the former, the forward model relates the limb radiances to the vertical profile, while for the latter, the forward model also includes a DOAS retrieval to relate the DOAS effective-column abundances to the vertical profile.

Using the forward model, the weighting-function matrix needed in the optimal estimation equations is calculated as

$$\mathbf{K} = \frac{\partial F}{\partial \mathbf{x}} \quad (20)$$

and is of dimensions m (rows) \times n (columns). Each row of \mathbf{K} is a weighting function, which shows how a given measurement is sensitive to changes in each of the n profile values. In this work, matrix \mathbf{K} is derived by perturbing each element of \mathbf{x} in turn and calculating the resulting perturbation in each element of the measurement $\mathbf{y} = F(\mathbf{x}, \mathbf{b})$ calculated using the forward model without adding error.

Then, given a set of measurements \mathbf{y} , it can be shown [37] that for F a linear function of \mathbf{x} , the profile $\hat{\mathbf{x}}$ and its covariance \hat{S} can be retrieved using the optimal estimation equations

$$\hat{\mathbf{x}} = \mathbf{x}_0 + S_0 \mathbf{K}^T (\mathbf{K} S_0 \mathbf{K}^T + S_y)^{-1} (\mathbf{y} - \mathbf{K} \mathbf{x}_0) \quad (21)$$

$$\hat{S} = S_0 - S_0 \mathbf{K}^T (\mathbf{K} S_0 \mathbf{K}^T + S_y)^{-1} \mathbf{K} S_0 \quad (22)$$

Here \mathbf{x}_0 is the a priori estimate of the true profile \mathbf{x} with error covariance S_0 . These equations combine the virtual measurement obtained from the a priori information with the real measurements to give the best estimate of the profile and its covariance. In practice, these equations are solved sequentially, using each scalar measurement y_i , $i = 1, \dots, m$, in turn, to improve the estimate of $\hat{\mathbf{x}}$ from the initial guess \mathbf{x}_0 through m intermediate values to the final solution.

The retrieved profile $\hat{\mathbf{x}}$ is related to the true profile \mathbf{x} by

$$\hat{\mathbf{x}} = I(\mathbf{y}, \mathbf{b}, \mathbf{c}) = I(F(\mathbf{x}, \mathbf{b})) = T(\mathbf{x}, \mathbf{b}, \mathbf{c}) \quad (23)$$

where I is the inverse model defining the retrieved profile $\hat{\mathbf{x}}$ in terms of the measurements \mathbf{y} , \mathbf{c} is a vector of parameters used in the retrieval, and T is the transfer function relating the retrieved profile to the true profile. The matrix of averaging kernels is then defined as

$$\mathbf{A} = \frac{\partial T}{\partial \mathbf{x}} = \left(\frac{\partial I}{\partial \mathbf{y}} \right) \left(\frac{\partial F}{\partial \mathbf{x}} \right) = \mathbf{D} \mathbf{K} \quad (24)$$

where \mathbf{D} is the matrix of contribution functions, which can also be calculated using the equation

$$\mathbf{D} = S_0 \mathbf{K}^T (\mathbf{K} S_0 \mathbf{K}^T + S_y)^{-1} \quad (25)$$

Each column of \mathbf{D} represents the contribution to the solution due to a unit change in the corresponding element of \mathbf{y} , and can illustrate how an error in a measurement y_i will lead to a compensating series of errors in $\hat{\mathbf{x}}$.

The retrieved profile at a given altitude, \hat{x}_j , is equal to the average of true profile \mathbf{x} weighted by the corresponding row of \mathbf{A} , with the width of the primary peaks of the averaging kernels providing a qualitative measure of the vertical resolution. The maximum possible value for n is m , i.e., the profile can only be retrieved at as many altitudes as there are measurements. The value of n is usually chosen to be less than m and can be arbitrarily set to minimize the vertical resolution, the noise on the retrieval, or some linear combination of the two [40,41].

Two approaches have been taken in developing a retrieval algorithm for OSIRIS based on optimal estimation. The first uses the limb radiances at discrete wavelengths as the measurements, and the second applies the DOAS technique to convert the radiances to effective-column abundances that are then used as the measurements. The results of applying each of these approaches to retrieve vertical profiles of trace-gas concentrations is described in Sect. 4.

3.2. Differential optical absorption spectroscopy

The second approach to the retrieval of local vertical concentration profiles (in molecules/cm³) involves first deriving the effective-column abundance (in molecules/cm²) along each OSIRIS limb-viewing line of sight using the DOAS method. From an analysis of how these effective-column abundances vary as a function of tangent height, the vertical profile can be obtained by again using optimal estimation. The DOAS technique is widely used for the detection of stratospheric constituents from the ground by measuring their absorption of sunlight scattered from the zenith sky [42]. Differential optical absorption spectroscopy offers several advantages for the analysis of OSIRIS UV–visible spectra

- (i) The spectra are recorded over a wide spectral range, allowing several species to be detected simultaneously, increasing the sensitivity to weak absorptions, and providing accurate discrimination between different absorbing trace gases.
- (ii) A ratio of the spectrum of interest to a reference spectrum is calculated, eliminating solar Fraunhofer structure, the instrument response function, and the need for an absolute instrument calibration.
- (iii) The use of the differential optical depth and differential absorption cross sections removes those spectral features that are smoothly varying functions of wavelength, particularly those due to Rayleigh and Mie scattering.

A brief discussion of the application of DOAS to OSIRIS spectra is instructive, as it provides some insight into the viewing geometry. First, consider the simple case of a solar occultation (note: OSIRIS will not be operated in this mode), which is described in greater detail by McDade et al. [43]. The Beer–Bouguer–Lambert law, (see, for example, ref. 44), gives the transmitted solar intensity when the line-of-sight, defined by tangent height z_{tan} , passes through the atmosphere

$$\begin{aligned} \frac{I(\lambda, z_{\text{tan}})}{I_0(\lambda)} &= \exp \left[- \left(D_{\text{Ray}}(\lambda, z_{\text{tan}}) + D_{\text{Mie}}(\lambda, z_{\text{tan}}) + \sum_i \sigma_i(\lambda) C_i(z_{\text{tan}}) \right) \right] \\ &= \exp [-D(\lambda, z_{\text{tan}})] \end{aligned} \quad (26)$$

where $I_0(\lambda)$ is the intensity of the unattenuated solar radiation, $D(\lambda, z_{\text{tan}})$ is the total optical depth along the line of sight through z_{tan} , $\sigma_i(\lambda)$ is the absorption cross section (cm²/molecule) of trace-gas i , and $C_i(z_{\text{tan}})$ is the column abundance along the line of sight (molecules/cm²). The extinction due to scattering is represented by the Rayleigh and Mie optical depths $D_{\text{Ray}}(\lambda, z_{\text{tan}})$ and $D_{\text{Mie}}(\lambda, z_{\text{tan}})$, which are slowly varying functions of wavelength, unlike the absorption cross sections, which are typically rich in spectral structure.

The standard DOAS approach assumes that each of the absorption cross sections can be represented as the sum of a component that varies slowly with wavelength, $\sigma_i^S(\lambda)$, and a differential component, $\sigma_i^D(\lambda)$, that varies rapidly with wavelength. The total optical depth can then be resolved into its own slowly and rapidly varying components

$$D^S(\lambda, z_{\text{tan}}) = \sum_i \sigma_i^S(\lambda) C_i(z_{\text{tan}}) + D_{\text{Ray}}(\lambda, z_{\text{tan}}) + D_{\text{Mie}}(\lambda, z_{\text{tan}}) \quad (27)$$

Fig. 4. Ozone weighting functions for limb radiances at 506 nm, using background aerosol, albedo = 0.3, SZA = 80°, scattering angle = 90°, a 5% perturbation, a 1 km measurement grid, and a 2 km profile grid.

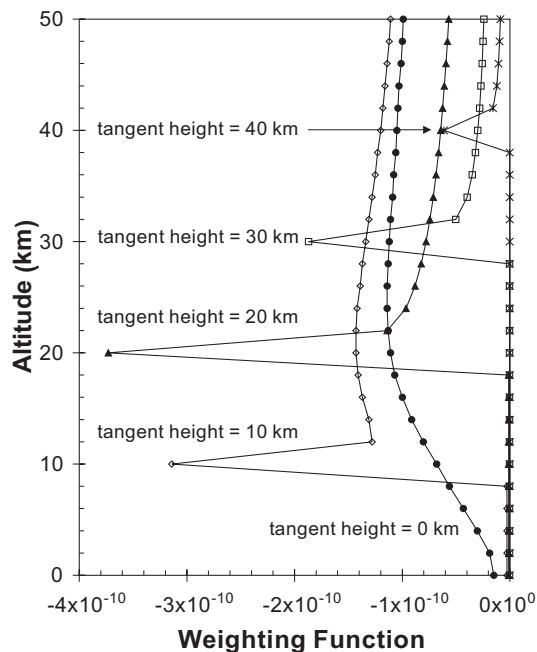
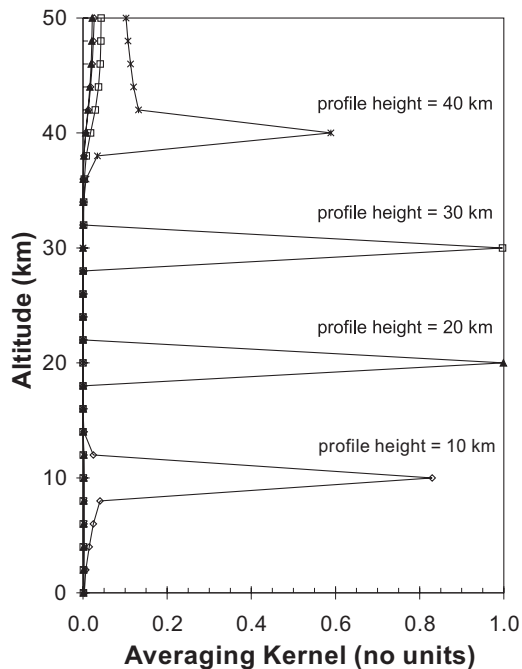


Fig. 5. Ozone-averaging kernels for limb radiances at 506 nm using background aerosol, albedo = 0.3, SZA = 80°, scattering angle = 90°, a 5% perturbation, a 1 km measurement grid, and a 2 km profile grid.

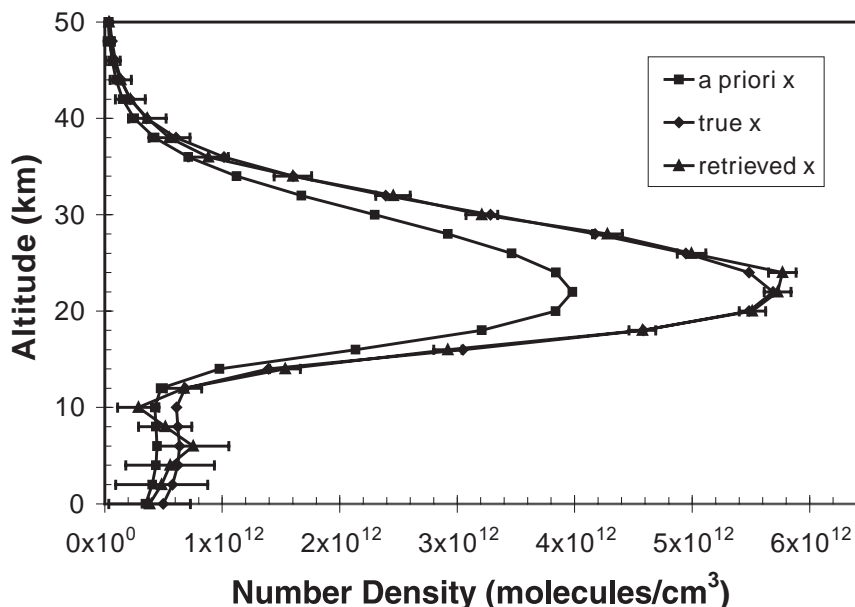


$$D^D(\lambda, z_{\text{tan}}) = \sum_i \sigma_i^D(\lambda) C_i(z_{\text{tan}}) \quad (28)$$

This last equation can be used to obtain the column abundances of the absorbing trace gases by fitting the differential cross sections of the relevant species to the measured differential spectrum.

In the case of solar occultation, DOAS should provide the actual column abundances along the line-of-sight, so that the concentration profiles can be obtained from a conventional matrix inversion using the geometric path lengths as the appropriate weighting functions. However, in the case of scattered-sunlight measurements, such as those that will be made by OSIRIS, it is not always clear what the weighting functions are, nor is it entirely obvious what the effective-column abundances represent. For example, the effective-column abundances obtained from the DOAS analysis of simulated limb radiances provide values that are significantly smaller than the geometric line-of-sight abundances [43]. This may seem surprising since it is often assumed that the DOAS abundances should in fact be larger because the sunlight passes through the atmosphere once on the way in to each scattering point and once again on the way out to the satellite instrument. However, this is an oversimplification. At lower tangent heights, Rayleigh-scattering extinction along the signal integration path reduces the effective-column abundances relative to the true (geometric) column abundances along the instrument line-of-sight. At higher tangent heights, in the absence of significant Rayleigh extinction, the effective-column abundances are still smaller than the geometric columns. This is because the elements on the near side of the limb are sampled by the total signal originating from beyond them (i.e., from below down to the tangent point and then up on the far side of the limb and out to space), whereas the same altitude elements on the far side are only sampled by the integrated signal originating from above, which for an exponential atmosphere is much smaller.

Fig. 6. Ozone number-density profiles retrieved on a 2 km grid using optimal estimation applied to limb radiances at 506 nm taken from Fig. 3. The error bars indicate the retrieved standard deviation corresponding to each retrieved density.



In the case of OSIRIS, which will measure UV–visible radiation scattered from the limb, the external source of radiation can be effectively regarded as a multitude of internal sources along the instrument line-of-sight, as described by McDade et al. [43]. Following their approach and taking into account all contributions along the line-of-sight, we can define the ratio

$$\begin{aligned}
 R(\lambda, z_{\text{tan}}) &= -\ln \left[\frac{I(\lambda, z_{\text{tan}})}{I(\lambda, z_{\text{ref}})} \right] \\
 &= \sum_i \sigma_i^D(\lambda) C_i(z_{\text{tan}}) + \left[\sum_i \sigma_i^S(\lambda) C_i(z_{\text{tan}}) + D_{\text{Ray}}^{\text{out}}(\lambda, z_{\text{tan}}) \right. \\
 &\quad \left. + D_{\text{Mie}}^{\text{out}}(\lambda, z_{\text{tan}}) - \ln [B(\lambda, z_{\text{tan}})] \right] \quad (29)
 \end{aligned}$$

Here, $I(\lambda, z_{\text{tan}})$ is the radiance observed at tangent height z_{tan} , $D_{\text{Ray}}^{\text{out}}(\lambda, z_{\text{tan}})$ and $D_{\text{Mie}}^{\text{out}}(\lambda, z_{\text{tan}})$ represent the effective Rayleigh and Mie optical depths for the out-going path, and $B(\lambda, z_{\text{tan}})$ is a scattering term appropriate for this tangent height. $C_i(z_{\text{tan}})$ is now the effective-column abundance of the absorbing trace-gas i along the line-of-sight that is determined by absorption on the way in from the Sun to the scattering point and by absorption on the way out from the scattering point towards OSIRIS.

Assuming that $B(\lambda, z_{\text{tan}})$ is a slowly varying function of wavelength, as it would be for incoming Rayleigh and Mie extinction and Rayleigh scattering, $R(\lambda, z_{\text{tan}})$ can be resolved into components that vary rapidly and slowly with wavelength. The former can again be assigned to the rapidly varying component of the absorber optical depth. Then for more than one absorber and multiple wavelength observations, the effective-column abundances of all the absorbers can be obtained by least-squares fitting of their differential cross sections to the differential ratio spectrum using

$$R^D(\lambda, z_{\text{tan}}) = \sum_i \sigma_i^D(\lambda) C_i(z_{\text{tan}}) \quad (30)$$

Fig. 7. The ratio of the retrieved to the true ozone profile using limb radiances at a single wavelength (506 nm) and at five wavelengths (483, 498, 506, 520, and 532 nm), with the retrievals performed on 1, 2, and 5 km grids.

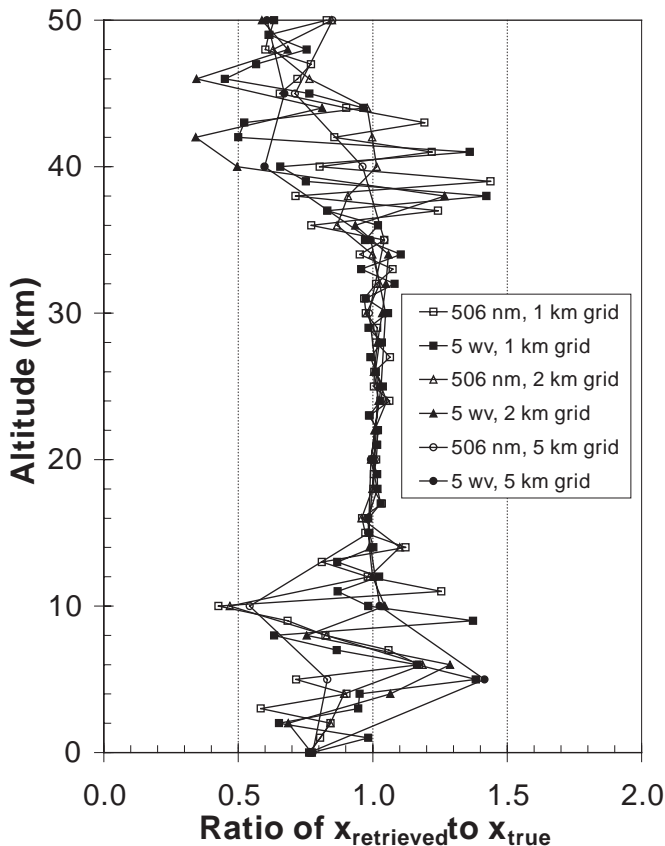


Fig. 8. DOAS calculation of the optical depth and the differential optical depth for a tangent height of 20 km, using limb radiances from 450 to 550 nm with background aerosol, albedo = 0.3, SZA = 80°, scattering angle = 90°, and the OSIRIS DM instrument response and noise.

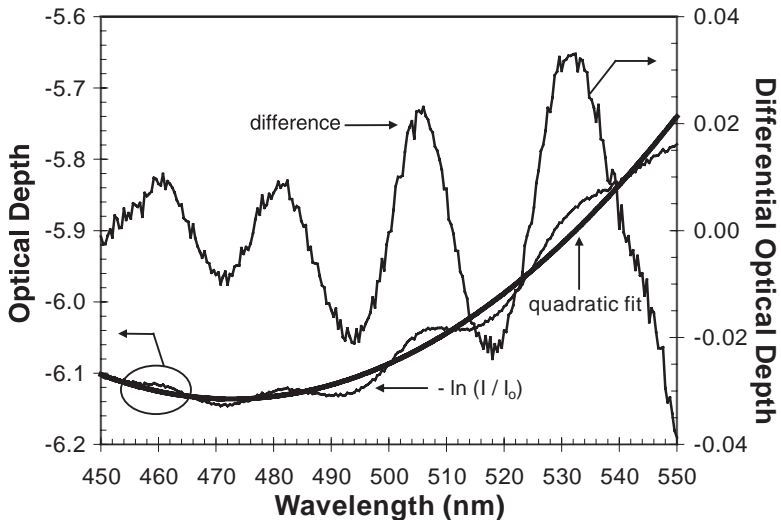


Fig. 9. (a) The differential optical depth for a tangent height of 20 km in the spectral range used for ozone, and the DOAS least-squares fit to this simulated “measurement”. (b) The scaled differential absorption cross sections for ozone, NO₂, and OClO, and the scaled differential Rayleigh cross section derived from the least-squares fit.

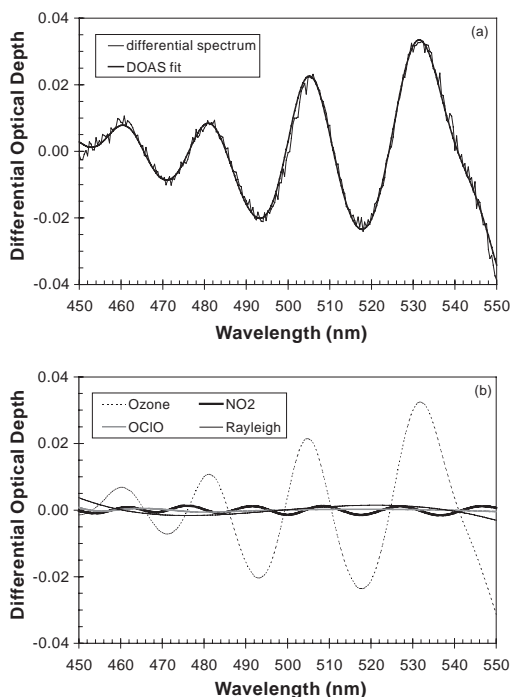
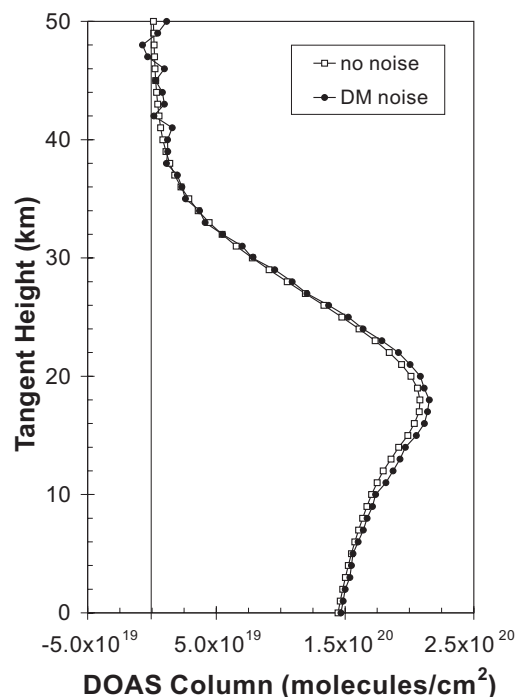


Fig. 10. DOAS ozone effective-column abundances derived using limb radiances from 450 to 550 nm on a 2 km grid with and without the OSIRIS DM instrument noise added to the radiances, although not to the 70 km reference spectrum.



Optimal estimation can then be applied to these DOAS effective-column abundances to retrieve vertical profiles of concentration.

4. Results

4.1. Application of optimal estimation to limb radiances

The first step in retrieving a vertical profile from radiances was to use the forward model to generate simulated measurements of limb radiance, $y(\lambda, z_{\text{tan}}, \mathbf{x})$, as a function of tangent height for a specified wavelength (or wavelengths) and a given vertical profile of the species of interest. The weighting-function matrix was calculated for ozone by perturbing its vertical profile one altitude at a time, regenerating the limb radiances, and calculating the change in radiance at every tangent height for the change in species concentration at every profile altitude. Figure 4 shows some typical weighting functions, in this case, those obtained for ozone at 506 nm using a +5% perturbation of the ozone profile. The corresponding averaging kernels are shown in Fig. 5, providing an indication of the vertical resolution of the retrieval. Given an a priori estimate of the true profile, a set of synthetic “measured” limb radiances, and a priori and measurement-noise covariance matrices, the optimal estimation equations were then applied to retrieve the vertical profile and its covariance for the minor species.

For this study, the limb radiances were calculated from 0 to 50 km using a 0.5 km grid, but output as measurements on a 1 km grid. Random measurement error ε_i was added to each measurement y_i , such that ε_i lay on the Gaussian curve for which the standard deviation σ_i was determined by the noise terms

Fig. 11. Ozone weighting functions for DOAS effective-column abundances derived using limb radiances from 450 to 550 nm, a 5% perturbation, background aerosol, albedo = 0.3, SZA = 80°, scattering angle = 90°, a 1 km measurement grid, and a 2 km profile grid.

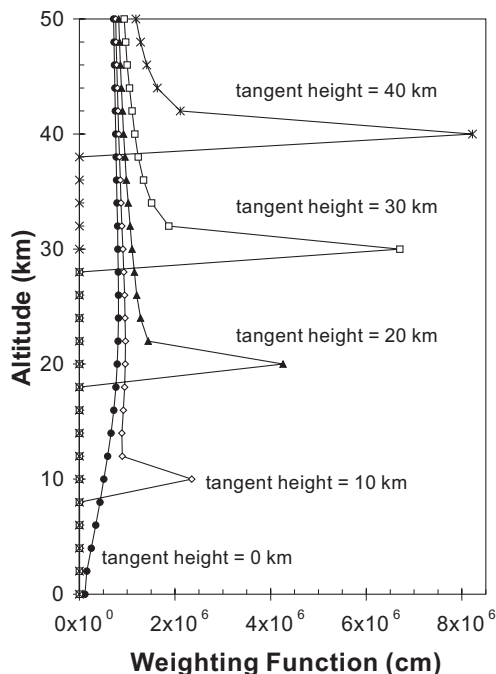
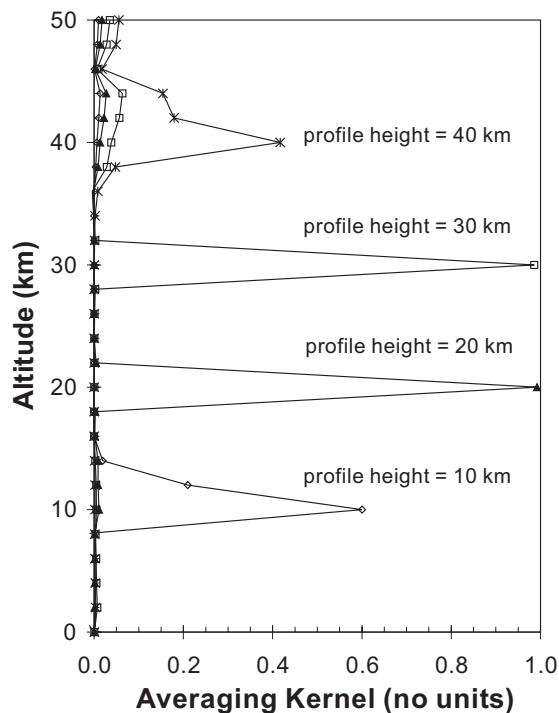


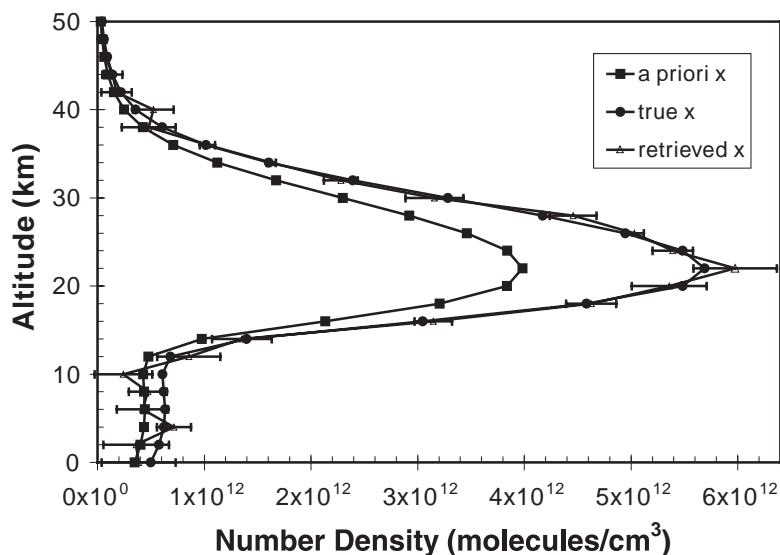
Fig. 12. Ozone-averaging kernels for DOAS effective-column abundances derived using limb radiances from 450 to 550 nm, a 5% perturbation, background aerosol, albedo = 0.3, SZA = 80°, scattering angle = 90°, a 1 km measurement grid, and a 2 km profile grid.



calculated using (18); the measurement-error covariance matrix S_y was then defined to have diagonal elements σ_i^2 with no interchannel correlation. For all the results discussed below, background aerosol was assumed, the surface albedo was set to 0.3, the scattering angle was fixed at 90°, and the solar zenith angle was fixed at 80°. The a priori profile was chosen to be 70% of the true profile, with a diagonal error covariance matrix whose elements were 100% of the a priori profile, thus giving the initial guess a low weighting. Retrievals were performed for ozone in the Chappuis band using radiances at a single wavelength (506 nm) and at a set of five wavelengths (483, 498, 506, 520, 532 nm) for which the ozone differential absorption cross section is either a maximum or a minimum. Values of 1, 2, and 5 km were used for the vertical resolution of the retrieved profile.

The initial results of these calculations indicated that the problem was nonlinear. Thereafter, the forward model was linearized about a reference profile, chosen to be the same as the a priori profile. When the forward model is linearized in this way, the retrieved profile for ozone is in excellent agreement with the true profile between 0 and 50 km for the case of no noise, and good results are also obtained when DM noise is added to the radiances. This is seen in Fig. 6, where the ozone profile retrieved on the 2 km grid using just the 506 nm radiances is clearly an improvement on the initial guess. The accuracy of the retrievals is improved by using limb radiances at five wavelengths instead of just one, and a further improvement is obtained at the expense of the vertical resolution of the retrieved profile. This is illustrated in Fig. 7, which shows the ratio of the retrieved ozone profile to the true profile for six cases: using limb radiances at 506 nm vs. limb radiances at 483, 498, 506, 520, and 532 nm and retrieving ozone on 1, 2, and 5 km grids. It is also clear from this figure that for all six cases the best

Fig. 13. Ozone number-density profile retrieved on a 2 km grid using optimal estimation applied to DOAS effective-column abundances derived using radiances from 450 to 550 nm.



agreement between the retrieved and true profiles is in the region of maximum ozone concentration. The differences between the two profiles are within $\pm 10\%$ for 15–35 km on the 1 km grid, $\pm 10\%$ for 12–34 km on the 2 km grid, and $\pm 5\%$ for 15–35 km on the 5 km grid. Below 15 km and above 35 km, where the ozone concentration decreases significantly, the retrieved profiles are in much poorer agreement with the true ozone number density.

4.2. Application of optimal estimation to DOAS effective-column abundances

4.2.1. Results for ozone

The DOAS technique as described in Sect. 3.2 was applied to obtain effective-column abundances from limb-radiance spectra generated using the forward model. Figure 8 illustrates how the term $R(\lambda, z_{\text{tan}})$ was obtained by making a ratio of the limb radiance at 20 km with that at 70 km (see (29)). The spectral structure in the 450–550 nm region shown is primarily due to absorption by ozone, making this a suitable region for deriving DOAS effective-column abundances for this trace gas. For each tangent height, $R(\lambda, z_{\text{tan}})$ was resolved into slowly and rapidly varying components by fitting a second-order polynomial to it and subtracting the resulting smooth curve, equivalent to $R^S(\lambda, z_{\text{tan}})$, to obtain the differential component $R^D(\lambda, z_{\text{tan}})$ required for the DOAS fit (see (30)). The same procedure was used to generate the rapidly varying, or differential cross sections, $\sigma_i^D(\lambda)$, of the absorbers.

The results of fitting the differential cross sections to $R^D(\lambda, z_{\text{tan}})$ are shown in Fig. 9. In Fig. 9a, the thin continuous line indicates the measured values for $R^D(\lambda, z_{\text{tan}})$ and the thick continuous line indicates the least-squares fit obtained using the individual fitting components that are shown in Fig. 9b. For this particular simulation (20 km tangent height, 450–550 nm) the fitting coefficients provided effective-column abundances of 2.09×10^{20} (7760 Dobson units), 1.18×10^{17} , and 2.72×10^{16} molecules/cm² for ozone, NO₂, and OCIO, respectively. Note that a differential Rayleigh “cross section” is also included in the DOAS fit, as the second-order polynomial does not accurately remove the smooth quartic nature of Rayleigh extinction over a wide spectral range. This procedure was repeated using simulated limb-radiance measurements at tangent heights from 0 to 50 km. The resulting vertical profiles of the ozone effective-column abundance are presented in Fig. 10, with and without DM noise added to the radiances. The DM instrument response and noise were applied to all the limb-radiance spectra; however, only

Fig. 14. The ratio of the retrieved to the true ozone profile, with the retrievals performed on 1, 2, and 5 km grids using optimal estimation applied to DOAS effective-column abundances for radiances from 450 to 550 nm.

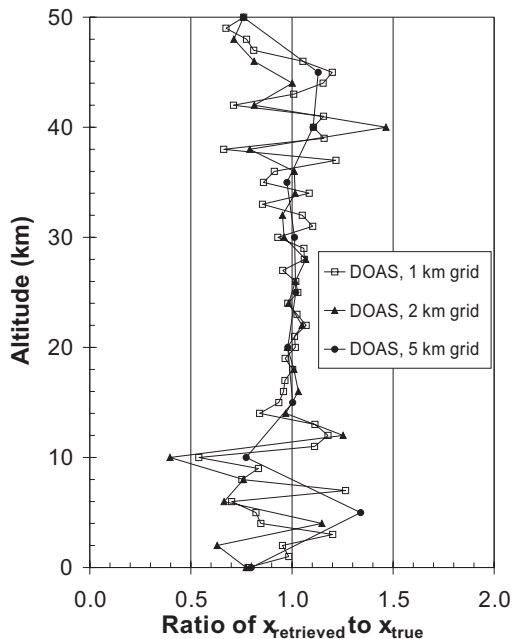
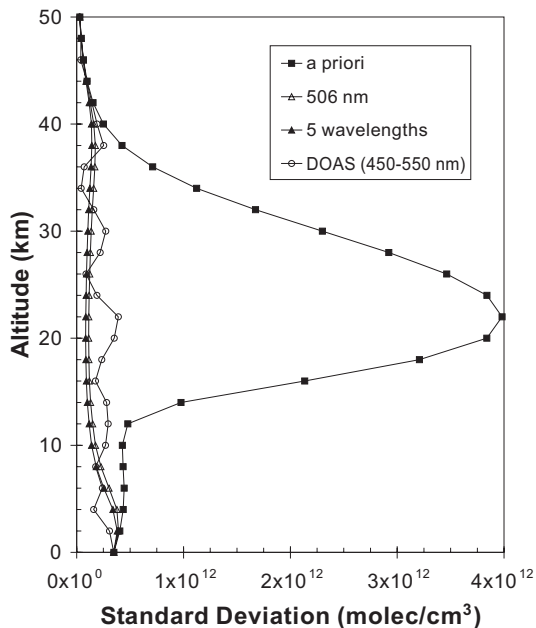


Fig. 15. Comparison of the standard deviation profiles retrieved for the ozone number-density profiles on a 2 km grid using limb radiance at 506 nm, limb radiances at five wavelengths, and DOAS ozone effective-column abundances derived from 450 to 550 nm.



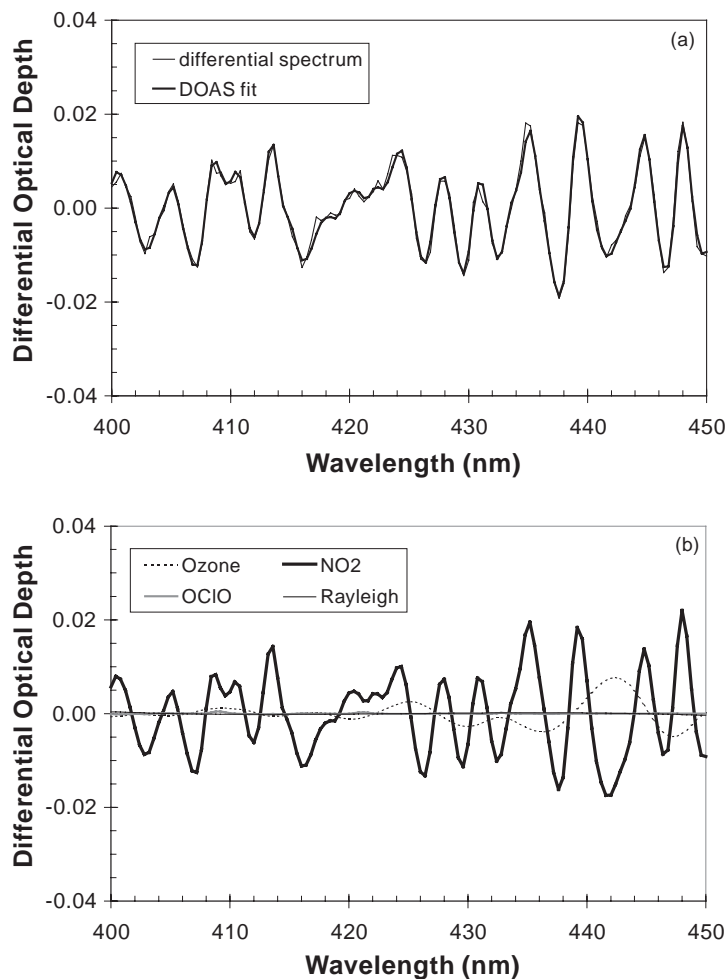
the DM instrument response was applied to the 70 km DOAS reference spectrum. Because of the low signal level at 70 km, adding DM noise to a single reference spectrum generated large errors in the retrieved DOAS effective-column abundances and hence in the retrieved profiles. In practice, the OSIRIS reference spectrum will be obtained by averaging a number of high-altitude limb radiances and optimizing the signal-to-noise ratio.

With the DOAS algorithm integrated into the combined forward-model optimal-estimation code, OE was then applied to the DOAS effective-column abundances to retrieve vertical profiles. With this procedure, the forward model was used to generate limb-radiance spectra, $I(\lambda, z_{\text{tan}}, \mathbf{x})$, from which DOAS ozone effective-column abundances, $C_i(z_{\text{tan}})$, were derived. These became the measurements $\mathbf{y}(z_{\text{tan}}, \mathbf{x})$ in the OE retrieval. The weighting-function matrix was then obtained by

- (i) perturbing the input ozone profile, \mathbf{x} , one altitude at a time,
- (ii) regenerating the limb-radiance spectra (no DM noise) for each perturbed profile,
- (iii) deriving the corresponding perturbed DOAS effective-column abundances for each perturbed profile, and finally
- (iv) calculating the change in ozone effective-column abundance at every tangent height for the change in ozone concentration at every profile altitude.

The computation of weighting functions for DOAS effective-column abundances is thus more lengthy than that for limb radiances. Figure 11 shows the weighting functions derived for ozone using DOAS applied to limb radiances from 450 to 550 nm. These are similar to those in Fig. 4, peaking at the relevant tangent height above ~ 10 km; however, their magnitude increases rather than decreases with altitude,

Fig. 16. (a) The differential optical depth for a tangent height of 20 km in the spectral range used for NO₂, and the DOAS least-squares fit to this simulated measurement. (b) The scaled differential cross sections derived from the least-squares fit.

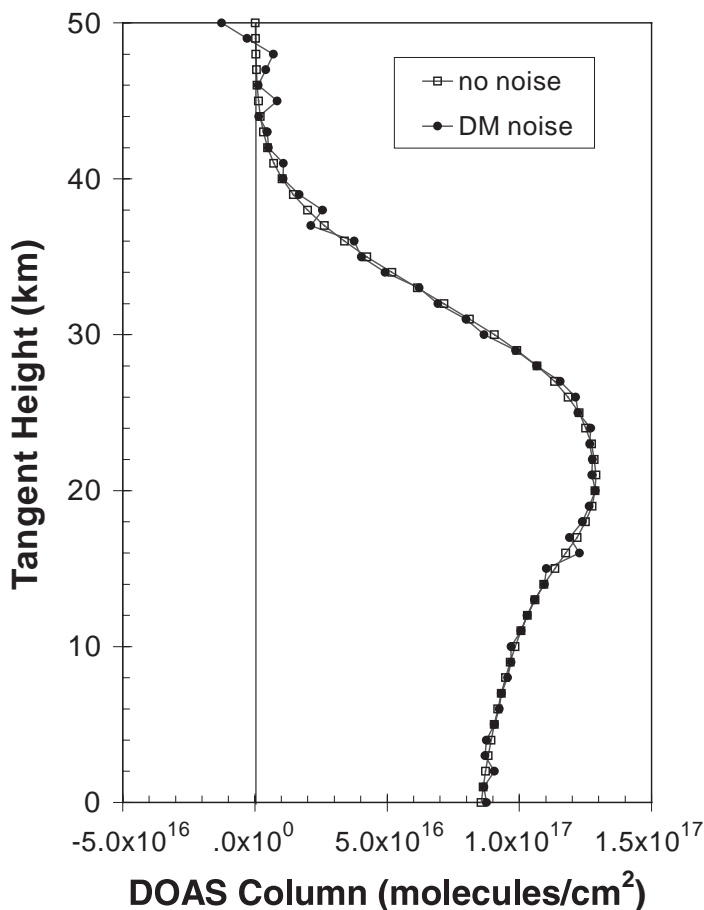


indicating that the sensitivity of DOAS effective-column abundances to changes in ozone density is greater at higher tangent heights. Figure 12 presents the corresponding averaging kernels, which exhibit a similar vertical resolution (~ 2 km FWHM) to those in Fig. 5.

As was done in applying OE to the radiances, the a priori profile was chosen to be 70% of the true profile, with a diagonal error covariance matrix whose elements were 100% of the a priori profile. Again, for the results discussed below, background aerosol was assumed, the surface albedo was set to 0.3, the scattering angle was 90° , and the solar zenith angle was fixed at 80° . A set of “measured” effective-column abundances was generated on a 1 km grid from 0 to 50 km, and then the OE equations were applied to retrieve the ozone profile \hat{x} and its covariance \hat{S} .

The ozone number-density profile retrieved by applying DOAS-OE is shown in Fig. 13 for the case of a 2 km grid, while the ratio of the retrieved profile to the true profile is shown in Fig. 14 for 1, 2, and 5 km grids. The ozone profile closely resembles those obtained using one and five limb radiances (cf. Fig. 6). The agreement between the retrieved and true profiles is within $\pm 15\%$ for 15–36 km on the 1 km grid (and within $\pm 10\%$ for all but two points in this range), $\pm 7\%$ for 14–36 km on the 2 km grid, and

Fig. 17. DOAS NO₂ effective-column abundances derived using limb radiances from 400 to 450 nm (for background aerosol, albedo = 0.3, SZA = 80°, scattering angle = 90°) with and without the OSIRIS DM instrument noise added to the radiances, although not to the 70 km reference spectrum.



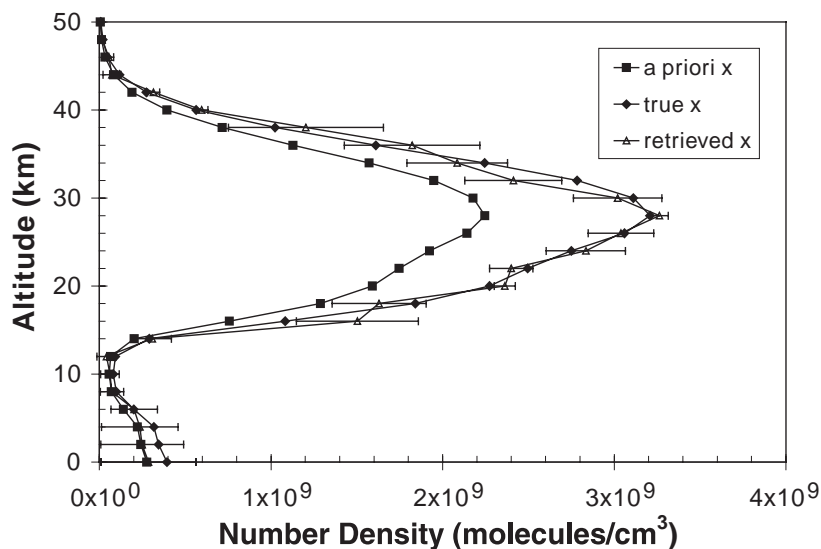
$\pm 5\%$ for 15–35 km on the 5 km grid. This is again very similar to the limb-radiance results that were given in Fig. 7. To further compare the information content of the DOAS effective-column abundances with that of the limb radiances, the retrieved standard deviation profiles for the three retrievals on the 2 km grid are shown in Fig. 15. Clearly, all three reduce the uncertainty in the profile significantly relative to the uncertainty in the a priori profile, with the DOAS retrieval exhibiting greater variability with altitude.

4.2.2. Results for NO₂, BrO, and OCIO

The same DOAS-OE approach was applied to the retrieval of number-density profiles of NO₂, BrO, and OCIO. Effective column abundances for each species were first obtained using DOAS over 400 to 450 nm for NO₂, 340 to 360 nm for BrO, and 350 to 400 nm for OCIO; these spectral bands were chosen as regions where the absorption of the gas of interest is greatest.

For NO₂, the differential spectrum (with DM noise) and the DOAS fit for a tangent height of 20 km are presented in Fig. 16a, with the corresponding components of this fit given in Fig. 16b. The full set of NO₂ effective column abundances is given in Fig. 17, with and without DM noise added to the radiances. The resulting vertical profile of NO₂ number density obtained by applying OE to the columns

Fig. 18. NO₂ number-density profile retrieved on a 2 km grid using DOAS-OE applied to radiances from 400 to 450 nm. The error bars indicate the retrieved standard deviation corresponding to each retrieved density.

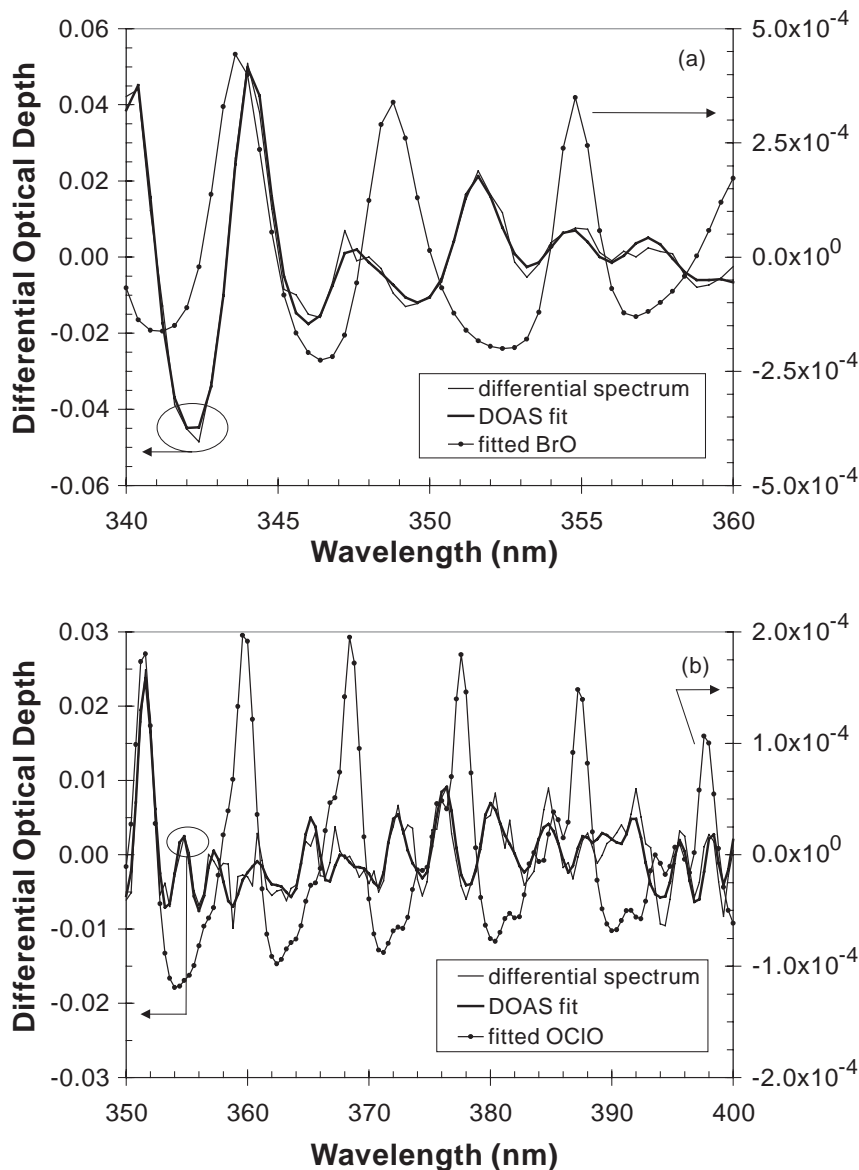


is in good agreement with the true profile (see Fig. 18), agreeing to within $\pm 13\%$ for altitudes between 18 and 36 km. The NO₂ weighting functions (not shown) peak at the relevant tangent heights above about 10 km, and the averaging kernels (not shown) are triangular with a FWHM of 2 km for altitudes about 10 km. These results suggest that it should be possible to obtain good NO₂ retrievals from OSIRIS limb-radiance spectra.

Initial efforts to retrieve BrO and OClO have been less successful. The results of performing a DOAS least-squares fit to the limb radiance (with DM noise) at a tangent height of 20 km are shown in Fig. 19. For both BrO and OClO, the fitted differential absorption of the gas is about two orders of magnitude less than the measured differential spectrum. As a consequence, the quality of the DOAS effective column abundances is particularly sensitive to the level of noise on the limb-radiance spectra. This is clearly seen in Fig. 20, where the BrO number-density profile retrieved using DOAS-OE is in excellent agreement with the true profile when noise-free radiances are used, but is significantly worse when DM noise is added to the radiances. For both cases, the retrievals are poor below about 15 km. For the radiances with noise, the retrieved BrO profile is almost identical to the a priori profile below 20 km and above 44 km. Between 22 and 42 km, the average magnitude of the difference between the retrieved and true profiles is 20% (cf. 30% for the a priori profile), with magnitudes ranging from 4.9% to 33.5%. The retrieval overestimates the BrO number density by about 30% at the peak.

A similar result was obtained for OClO (not shown). In the noise-free case, the retrieved number-density profile reproduces the true profile above 15 km. However, when noise is added to the radiances, the retrieved OClO profile remains the same as the a priori profile below 20 km and above 30 km and underestimates the true profile to a greater extent than the a priori profile between 22 and 28 km. Figures 21 and 22 shed some additional light on the reason for these poor retrievals. Figure 21 shows the weighting functions for BrO; although these peak at the tangent height for altitudes above 20 km, they include little information for tangent heights below 20 km. The rapid decrease in the weighting functions with decreasing tangent height below about 20 km can be attributed to the shorter wavelengths used in the retrievals. At 350 nm, the Rayleigh-scattering optical depth is about four times that at 500 nm, and thus light scattered into the OSIRIS line of sight at 350 nm undergoes significantly greater attenuation than that at longer wavelengths. The averaging kernels for BrO, seen in Fig. 22, are also striking; these have a small peak at the relevant profile altitude above 20 km, but all are very broad and all include a

Fig. 19. The differential optical depth, the DOAS least-squares fit, and the fitted differential cross section for a tangent height of 20 km in the spectral ranges used to retrieve (a) BrO and (b) OCIO.

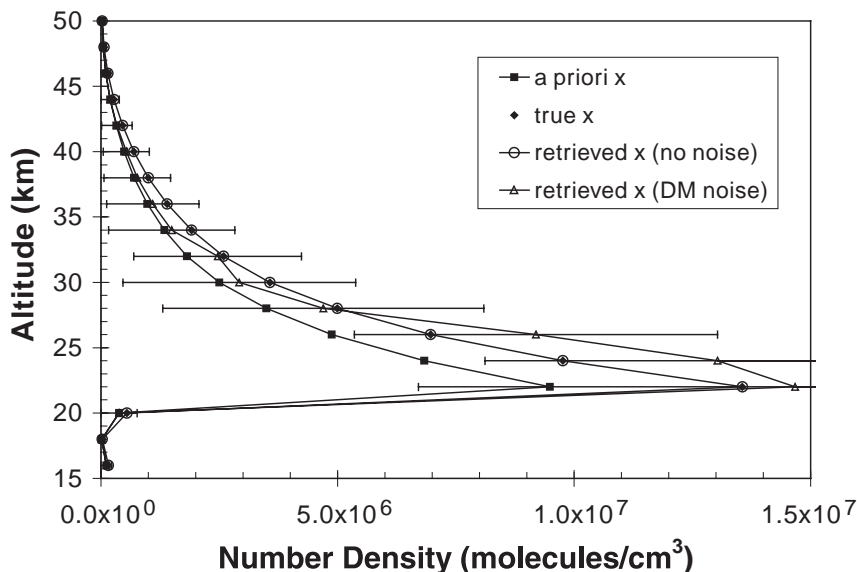


significant contribution from all altitudes above about 15 km. The weighting functions and averaging kernels for OCIO are similar to those for BrO. These retrieval parameters depend on the stratospheric density profiles of the trace gases; because these can have significant variability, further investigation of BrO and OCIO retrievals using other profiles will be pursued.

5. Conclusions

This paper describes two approaches to the retrieval of vertical profiles of trace-gas concentrations from UV-visible limb-radiance spectra that will be recorded by the OSIRIS instrument on the Odin satellite. A single-scattering radiative-transfer model has been developed for the simulation of UV-

Fig. 20. BrO number-density profile retrieved on a 2 km grid using DOAS-OE applied to radiances from 340–360 nm, with a 5% perturbation, background aerosol, albedo = 0.3, SZA = 80°, scattering angle = 90°, and a 1 km measurement grid. The error bars indicate the retrieved standard deviation corresponding to each retrieved density when DM noise is added to the radiances.



visible spectra of sunlight scattered from the limb. It uses partial spherical geometry, and in addition to absorption by ozone, NO₂, BrO, and OClO, it includes Mie scattering by stratospheric aerosols and a Lambertian surface contribution. For the results reported here, a solar zenith angle of 80°, a scattering angle of 90°, background aerosol, and an albedo of 0.3 were assumed as conditions that will be typical during OSIRIS observations. In addition, the OSIRIS instrument response and noise were applied to the calculated limb radiances using data obtained during calibration testing of the development model.

The two inversion methods investigated in this work involve the application of optimal estimation to (i) limb radiances at specific wavelengths, and (ii) DOAS effective column abundances derived from spectra over broader spectral ranges. Both approaches have been successfully applied to the retrieval of simulated ozone number densities. In the first case, OE was applied to limb radiances at a single wavelength and at a set of five wavelengths in the Chappuis band, and profiles were retrieved on 1, 2, and 5 km grids. With only one iteration of the inversion, the retrieved ozone profiles were within $\pm 10\%$ of the true profile for all six cases. The retrieved standard deviation on the profiles was significantly less than that on the a priori profile and was smaller for the set of five wavelengths than for the single wavelength. The accuracy of the retrieved ozone profile also improved as the vertical resolution decreased, with the ozone profile retrieved on the 5 km grid agreeing with the true profile to $\pm 5\%$ between 15 and 35 km.

With the second approach, DOAS effective-column abundances were first derived from the limb radiances in the 450 to 550 nm region of the ozone Chappuis band, and then OE was applied to these to retrieve number-density profiles. In this case, the retrieved profiles are within $\pm 15\%$, $\pm 7\%$, and $\pm 5\%$ (between about 15 and 35 km) on 1, 2, and 5 km grids, respectively. Overall, these results for ozone suggest that vertical profiles of concentration can be obtained to at least 10% accuracy in the middle stratosphere by applying OE to either OSIRIS limb radiances or to DOAS effective-column abundances derived from these radiances. Each has an advantage: the use of OSIRIS limb radiances results in a simpler inversion problem, whereas the use of the DOAS columns eliminates the need for accurate radiometric calibration of the radiances.

Good results were also obtained when DOAS-OE inversions were used to retrieve number-density

Fig. 21. BrO weighting functions for DOAS effective-column abundances derived using radiances from 340–360 nm, a 5% perturbation, background aerosol, albedo = 0.3, SZA = 80°, scattering angle = 90°, a 1 km measurement grid, and a 2 km profile grid.

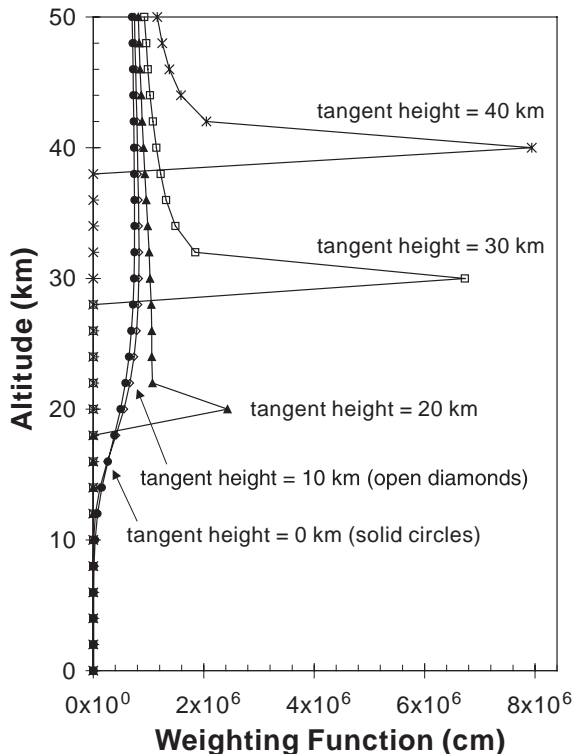
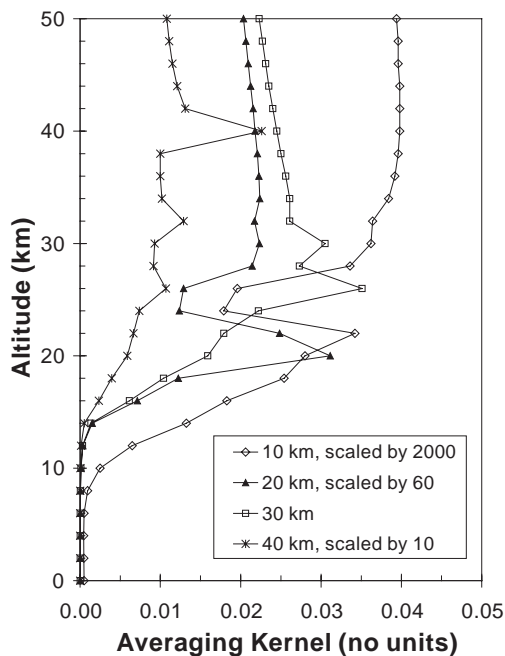


Fig. 22. BrO averaging kernels for DOAS effective-column abundances derived using radiances from 340–360 nm, a 5% perturbation, background aerosol, albedo = 0.3, SZA = 80°, scattering angle = 90°, a 1 km measurement grid, and a 2 km profile grid.



profiles for NO₂, with $\pm 13\%$ agreement between the retrieved and true profiles for altitudes from 18 to 36 km on a 2 km grid. Differential optical absorption spectroscopy–optimal estimation retrievals of BrO and OCIO reproduced the true profiles above about 15 km when the effective-column abundances were derived from noise-free radiances. However, when DM noise was added, the retrievals were poor, with the BrO profile improving only slightly on the a priori profile between 22 and 42 km, and the OCIO inversion providing a worse profile than the a priori between 22 and 28 km. This sensitivity to the noise on the radiances is due to the weak absorption of these two gases, which is less than 1% of the differential optical depth at a tangent height of 20 km. The resulting DOAS effective-column abundances derived from the radiances with noise exhibit significant random variability with tangent height, making the final number-density profiles unreliable.

The initial results of applying OE to simulated OSIRIS limb radiances and DOAS columns thus give encouraging results for ozone and NO₂; however, we must further assess the feasibility of BrO and OCIO retrievals. We anticipate that the latter will improve when the OSIRIS DM instrument-response function is replaced with the flight-model instrument function and when all 32 pixels in a column are added for each wavelength bin. In practice, it will also be possible to improve the signal-to-noise ratio of OSIRIS spectra by increasing the integration time and co-adding spectra.

The development of inversion methods for the retrieval of geophysical quantities from OSIRIS UV–visible spectra is an ongoing activity. Future work falls into two categories: improvements to the forward model and refinements of the retrieval algorithms. Potential modifications to the single-scattering model include the addition of atmospheric refraction, the Ring effect, polarization and its

dependence on solar zenith angle and scattering angle, and temperature-dependent cross sections. In addition, a number of multiple-scattering radiative-transfer models are available [45,46], which will allow the impact of multiple scattering on the weighting functions and retrievals to be investigated. Improvements to the inversion algorithms will include iterating the optimal estimation retrieval, adding off-diagonal elements to the measurement-noise covariance matrix, and investigating the use of the ratio $I(z)/I_0(70 \text{ km})$ as measurements. Other issues to be investigated include the effect of surface albedo on the DOAS effective-column abundances and on the retrievals and the feasibility of retrieving the surface albedo and aerosols. The testing and refinement of forward models and inversion methods for OSIRIS is thus continuing.

Acknowledgments

This work was supported by the Canadian Space Agency (CSA) and the Natural Sciences and Engineering Research Council of Canada (NSERC).

References

1. E.J. Llewellyn. *Can. J. Phys.* **80** (2002). This issue, the foreword.
2. D.P. Murtagh et al. *Can. J. Phys.* **80** (2002). This issue.
3. E.J. Llewellyn, D.A. Degenstein, I.C. McDade et al. OSIRIS – An application of tomography for absorbed emissions in remote sensing. Applications of photonic technology 2. *Edited by G.A. Lampropoulos and R.A. Lessard*. Plenum Press, New York. 1997. pp. 627–632.
4. J.C. Gille and J.M. Russell, III. *J. Geophys. Res.* **89**(D4), 5125 (1984).
5. F.W. Taylor, C.D. Rodgers, J.G. Whitney et al. *J. Geophys. Res.* **98**, 10 799 (1993).
6. F.T. Barath, M.C. Chavez, R.E. Cofield et al. *J. Geophys. Res.* **98**, 10 751 (1993).
7. D. Heath, A.J. Krueger, and H. Park. *In The Nimbus 7 users' guide*. *Edited by C.R. Madrid*. Management and Technical Services Company, Beltsville, Md. The Landsat/Nimbus Project, NASA/GSFC. August 1978. p. 175.
8. R.P. Cebula, H. Park, and D.F. Heath. *J. Atmos. Oceanic Technol.* **5**, 215 (1988).
9. M.P. McCormick. *Adv. Space Res.* **7**, 219 (1987).
10. C.T. McElroy, J.B. Kerr, D.I. Wardle et al. *Can. J. Phys.* **69**, 1123 (1991).
11. A. Hahne et al. The global ozone monitoring experiment (GOME) users manual. European Space Agency (ESA) SP-1182, ESTEC, Noordwijk, The Netherlands. September, 1995.
12. European Space Agency (ESA), GOME special issue, *Earth Observation Quarterly*, No. 58, and references therein. ESTEC, Noordwijk, The Netherlands. March, 1998.
13. D.W. Rusch, G.H. Mount, C.A. Barth, R.J. Thomas, and M.T. Callin. *J. Geophys. Res.* **89**(D7), 11 677 (1984).
14. G.H. Mount, D.W. Rusch, J.F. Noxon, J.M. Zawodny, and C.A. Barth. *J. Geophys. Res.* **89**(D1), 1327 (1984).
15. T. Aruga and D.F. Heath. *Appl. Opt.* **21**, 3047 (1982).
16. G.J. Romick, D.E. Anderson, Jr., J.F. Carbary, L.J. Paxton, D.M. Morrison, and C.-I. Meng. *SPIE Proc.* **2223**, 160 (1994).
17. R.D. McPeters, S.J. Janz, E. Hilsenrath, T.L. Brown, D.E. Flittner, and D.F. Heath. *Geophys. Res. Lett.* **27**, 2597 (2000).
18. D.E. Flittner, P.K. Bhartia, and B.M. Herman. *Geophys. Res. Lett.* **27**, 2601 (2000).
19. B.M. Herman, D.E. Flittner, R.D. McPeters, and P.K. Bhartia. *SPIE Proc.* **2582**, 88 (1995).
20. M.P. McCormick, W.P. Chu, J.M. Zawodny, L.E. Mauldin, and L.R. McMaster. *SPIE Proc.* **1491**, 125 (1991).
21. R.W.M. Hoogeveen, A.P.H. Goede, S. Slijkhuis, A. Selig, and J.P. Burrows. *SPIE Proc.* **2209**, 78 (1994).
22. A. Berk, L.S. Bernstein, and D.C. Robertson. Report No. F19628-86-C-0079. Air Force Geophysics Laboratory, Hanscom A.F.B., Mass. 1989. p. 38.
23. R. Lehtinen. Personal communication. 1996.
24. G. Witt, J.E. Dye, and N. Wilhelm. *J. Atmos. Terr. Phys.* **38**, 223 (1976).
25. R. Penndorf. *J. Opt. Soc. Am.* **47**(2), 176 (1957).

26. B. Edlen. *J. Opt. Soc. Am.* **43**(5), 339 (1953).
27. D.R. Bates. *Planet. Space Sci.* **32**(6), 785 (1984).
28. R.M. Goody and Y.L. Yung. *Atmospheric radiation*. 2nd. ed. Oxford University Press, Oxford, U.K. 1989.
29. M. Abramowitz and I.A. Stegun. *Handbook of mathematical functions*. National Bureau of Standards Applied Mathematics. Series 55. NBS, Washington, D.C. 1966.
30. B. Sturm. *In Oceanography from space*. Edited by J.F.R. Gower. Plenum, New York. 1981. pp. 267–279.
31. J.E.P. Eriksson, F. Merino, D.P. Murtagh, P. Baron, Ph. Ricaud, and J. de la Noë. *Can. J. Phys.* **80** (2002). This issue.
32. R.L. Kurucz, I. Furenlid, J. Brault, and L. Testerman. *Solar flux atlas from 296 to 1300 nm*. National Solar Observatory, Sunspot, N.Mex. 1984.
33. J.P. Burrows, A. Richter, A. Dehn, B. Deters, S. Himmelmann, S. Voigt, and J. Orphal. *J. Quantum Spectrosc. Radiat. Transfer*, **61**, 509 (1999).
34. J.P. Burrows, A. Dehn, B. Deters, S. Himmelmann, A. Richter, S. Voigt, and J. Orphal. *J. Quantum Spectrosc. Radiat. Transfer*, **60**, 1025 (1998).
35. A. Wahner, A.R. Ravishankara, S.P. Sander, and R.R. Friedl. *Chem. Phys. Lett.* **152**, 507 (1988).
36. A. Wahner, G.S. Tyndall, and A.R. Ravishankara. *J. Phys. Chem.* **91**, 2734 (1987).
37. C.D. Rodgers. *Rev. Geophys. Space Phys.* **14**, 609 (1976).
38. C.D. Rodgers. *J. Geophys. Res.* **95**(D5), 5587 (1990).
39. R. de Beek, R. Hoogen, V. Rozanov, and J.P. Burrows. *Ozone profile retrieval from GOME satellite data I: Algorithm description*. Proc. 3rd ERS Symposium, Florence, Italy. March 1997. ESA SP-414, Vol. II. 1997. pp. 749–754.
40. G.E. Backus and J.F. Gilbert. *Philos. Trans. R. Soc. London A*, **266**, 123 (1970).
41. B.J. Conrath. *J. Atmos. Sci.* **29**, 1262 (1972).
42. S. Solomon, A.L. Schmeltekopf, and R.W. Sanders. *J. Geophys. Res.* **92**, 8311 (1987).
43. I.C. McDade, K. Strong, C.S. Haley, J. Stegman, D.P. Murtagh, and E.J. Llewellyn. *Can. J. Phys.* **80** (2002). This issue.
44. F.H. Perrin. *J. Opt. Soc. Am.* **38**, 72 (1948).
45. E. Griffioen and L. Oikarinen. *J. Geophys. Res.* **105**(D24), 29 717 (2000).
46. C.A. McLinden, J.C. McConnell, E. Griffioen, and C.T. McElroy. *Can. J. Phys.* **80** (2002). This issue.